Electronic Supplementary Information

Carrier Relaxation and Exciton Dynamics in Chemical-Vapor-Deposited Two-Dimensional Hybrid Halide Perovskites

Dallar Babaian†, Daniel Hill†, Ping Yu†‡, and Suchismita Guha†‡*

†Department of Physics and Astronomy, University of Missouri, Columbia, MO 65211

‡ MU Materials Science and Engineering Institute, University of Missouri, Columbia, MO 65211

* Corresponding Author E-mail: guhas@missouri.edu

Contents

1. CVD growth of 2D perovskites

The chemical vapor deposition (CVD) growth was conducted in a double zone tube furnace from SAFTherm (model STG-100-12-2). The temperature profile of either zone can be independently controlled. Nitrogen was supplied to the reactor with a downstream precision mass flow controller from MTI Corporation that was used to mediate the flow rate of the gas. The 2D perovskite films were grown in two steps. First a film of PbI_2 (of thickness 40 nm) was deposited, which was then converted by PEAI and BAI vapors. For the conversion step, the deposition pressure was fixed to 0.1 atm with the sublimation temperature for the BAI and PEAI fixed at 170 °C. The nitrogen gas flow rate was set to 1000 sccm and 300 sccm for conversion in the BAI and PEAI vapors, respectively. The overall thickness of the perovskite films was approximately 180 nm. Details of the CVD growth and x-ray diffraction characterization of the films are found in Ref. [1]. The SnO_2 heterojunctions were formed by spin coating 20 μL of the tin oxide solution first at 500 rpm for 5 seconds then increasing to 2000 rpm for 20 seconds. It was subsequently annealed at 120^o C in atmosphere for 5 minutes. The thickness of the SnO_2 layer was 20 ± 5 nm.

2. Pump-probe spectroscopy setup

The fundamental 800 nm beam is produced by a regenerative amplifier (Spitfire Ace, Spectra Physics) with a repetition rate of 1kHz, 1 mJ single pulse energy, and pulse duration of 100 fs, seeded by a Ti:Sapphire laser (Mai Tai, Spectra Physics) and pumped by a Q-switched laser (ASCEND, Spectra Physics). The schematic of the experimental setup is shown in **Fig. S1**. The red and blue arrows depict the path of the 800 nm (fundamental) and 400 nm (pump) beams, respectively. The rainbow-colored arrows depict the path of the white light continuum probe beam. The 400 nm pump beam is generated by a Tripler (Minioptic Tech. inc.) using the amplified 800 nm fundamental beam as an input. In addition to the conversion from 800 nm to 400 nm, an additional 800 nm beam in the Tripler can be used for supercontinuum generation for the probe. A combination of a half wave plate and the first surface of a glass window sample at its Brewster angle are used to control the power of the 800 nm fundamental beam for the probe. The 800 nm fundamental beam then passes through a telescope to increase the beam size and produce a collimated beam. The white light supercontinuum (probe) is produced by focusing the collimated beam onto a 2 mm thick sapphire crystal (Thorlabs) via a parabolic mirror. The probe beam is then passed through a BG37 filter (Thorlabs) to block the remainder of the fundamental 800 nm wavelength and is focused to a spot size of about 1 mm onto the sample via a second parabolic mirror. The parabolic mirror pair is used to minimize the spherical and chromatic aberrations and to preserve the pulse width. Unlike transmission optics which may induce a time delay, the use of reflection optics in our setup after the super continuum generation eliminates the need to apply a post measurement chirp correction to the probe beam. The time delay between the pump and probe beam is achieved by using a delay line (ODL 220, Thorlabs) in the 400 nm pump beam path. An optical chopper (MC1F10HP, Thorlabs) is electronically synchronized to the laser pulses via the use of the chopper driver (MC2000B, Thorlabs). The chopper driver divides the 1 kHz frequency of the laser pulses by 5 which is then used to operate the outer (100) blades of the chopper at a 200 Hz which in turn operates the inner (10) blades of the chopper at a 20 Hz with a 50% duty cycle. In turn the pump beam switches on and off every 50 ms. The pump is then focused on the sample with a beam spot size of approximately 2 mm. A slight angular deviation between the pump and the probe beam incident at the sample ensures that the pump beam misses the

spectrometer. A collection lens after the sample focuses the probe beam onto a fiber optic cable which carries the light to the spectrometer (Flame, Ocean Optics). The spectrometer is consequently triggered via a 40 Hz electronic signal which is synchronized with the 20 Hz frequency of the chopper. The spectrometer is configured with an integration time of ~5-8 ms at a repetition rate of 40 Hz which results in successive pumped and not-pumped transmission spectra to be measured and stored.

A Python script was developed to interface with the delay line driver (pyLabLib package) as well as the spectrometer (python-seabreeze package) to automate the measurement process. The script allows for multiple parameters to be customized such as the range and step size of the delay line as well as the integration time and number of spectra per delay line to be stored. The current experimental set up allows for time delays of up to ~970 ps with a resolution of 67 fs. A secondary Python script was developed to sort and average the spectra stored during the measurement process. This script identifies and sorts the 100 spectra for each delay time between pumped and not-pumped spectra using the faint signal from the pump that is visible in the spectra. Then all the pumped and not-pumped spectra are averaged, and the differential spectra is calculated and stored for each delay time. The spectra are then used to create the time and wavelength dependent transient absorption spectroscopy (TAS) maps for each sample.

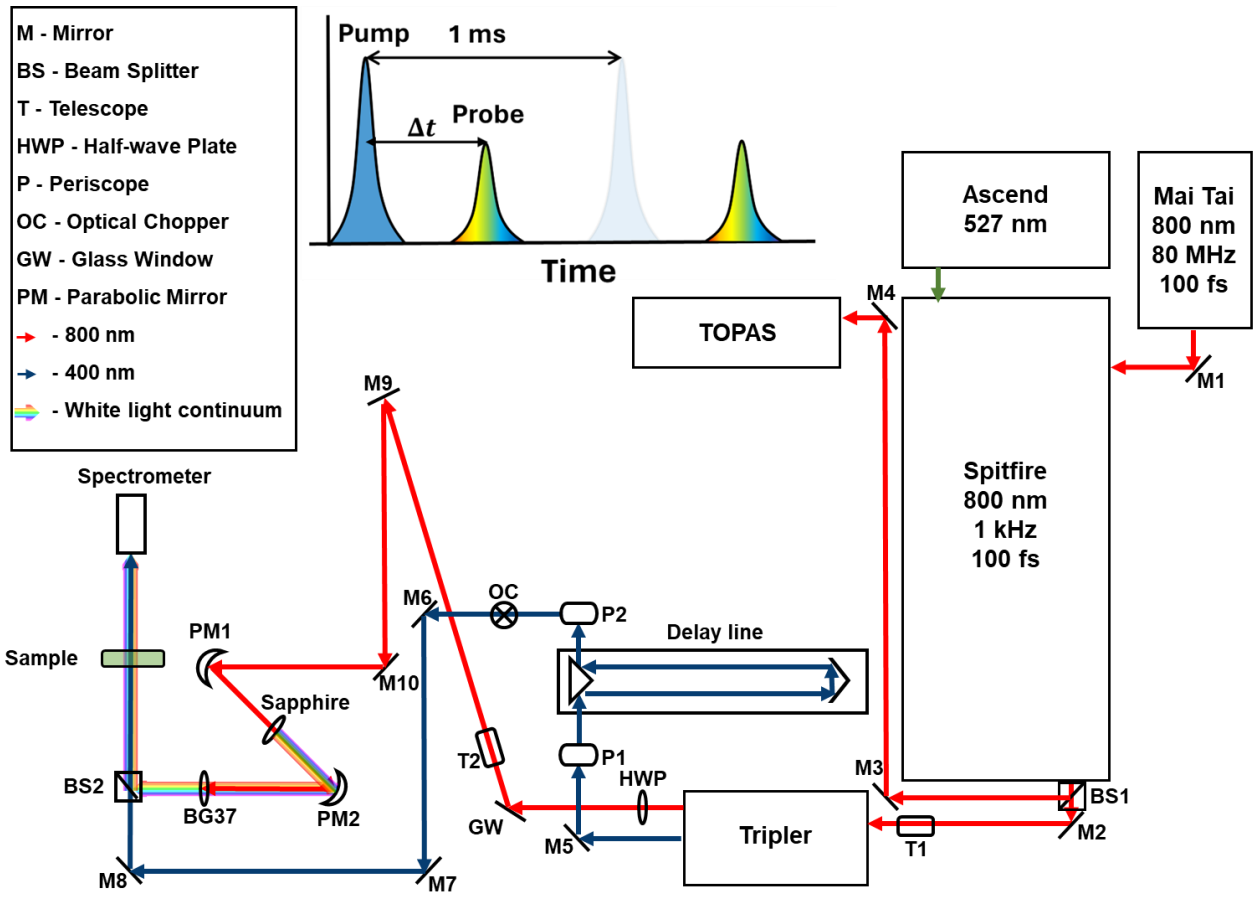

Fig. S1. Schematic of the experimental setup used for TAS measurements. The inset shows a simplified timing scheme of the experiment.

3. TRPL fits

The decay curve of the TRPL measurement can be fit by a set of exponential decay equations given by $\mathrm{f}(x) = \sum_n f_n(x)$ where, $f_n(x) = \frac{A_n}{\tau_n} e^{-x/\tau_n}$ where n is the number of lifetimes that best fit the decay, A_n is the amplitude and τ_n is the time constant of the decay. In a TRPL measurement the effect of the instrument response function (IRF) needs to be accounted for. The IRF can be written as a Gaussian function of width w and peak position of x_c as

$$f_{\mathrm{IRF}}(x) = \frac{1}{\sqrt{2\pi}w} e^{-(x-x_c)^2/2w^2}.$$

The equation best fitting the data is therefore the convolution of the IRF spectrum function (f_{IRF}) with the sum of the multiple exponential decay and can be written utilizing an error function,

$$\sum_n f_n(x) \times f_{\mathrm{IRF}}(x) = \sum_n \int_0^\infty f_n(x) f_{\mathrm{IRF}}(x - x')dx'$$
$$= \sum_n \frac{A_n}{2\tau_n} e^{\left[\frac{w^2}{2\tau_n^2} - \frac{x-x_c}{\tau_n}\right]} \left[1 + \mathrm{erf}\left(\frac{1}{\sqrt{2}}\left(\frac{x-x_c}{w} - \frac{w}{\tau_n}\right)\right)\right].$$

Similar to other perovskite nanocrystals,[2] the TRPL decay curves for our samples are best fit with two lifetimes (τ_1 and τ_2). The average PL lifetime is estimated from:

$$\tau_{\mathrm{avg}} = \frac{A_1\tau_1^2 + A_2\tau_2^2}{A_1\tau_1 + A_2\tau_2}.$$

A sample TRPL curve fit for PEA_2PbI_4 is plotted in **Fig. S2.** The fit results for all samples are provided in the table below.

Table. S1. The results of the TRPL fits are shown for all samples.

Sample	A_1	τ_1(ns)	A_2	τ_2(ns)	τ_{avg} (ns)
BA_2PbI_4	0.048 ± 0.001	0.095 ± 0.001	0.270 ± 0.0009	0.353 ± 0.001	0.341
SnO_2 + BA_2PbI_4	0.034 ± 0.0006	0.066 ± 0.001	0.228 ± 0.0005	0.287 ± 0.0009	0.280
PEA_2PbI_4	0.333 ± 0.0009	0.290 ± 0.0005	0.022 ± 0.0008	1.01 ± 0.04	0.425
SnO_2 + PEA_2PbI_4	0.312 ± 0.001	0.281 ± 0.0006	0.066 ± 0.001	0.77 ± 0.01	0.463

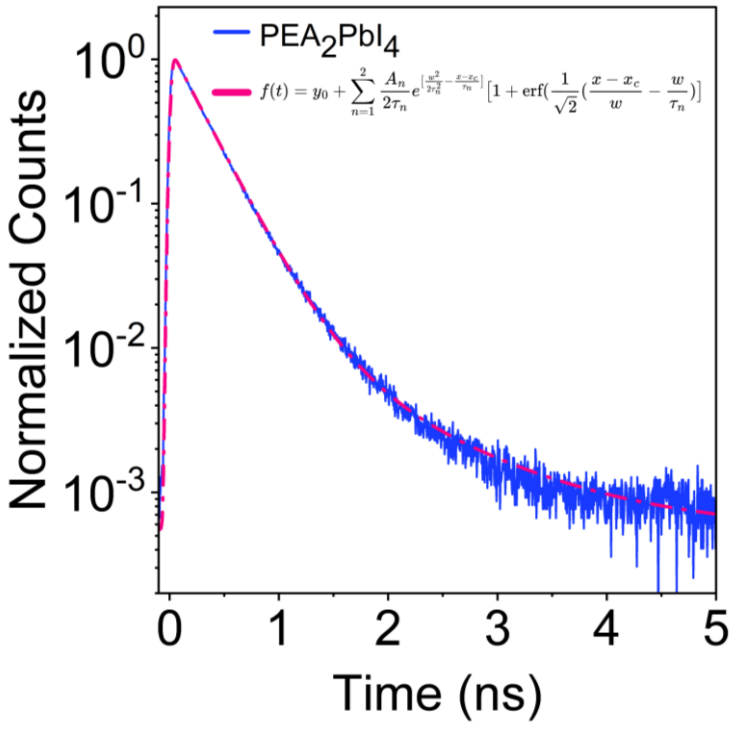

Fig. S2. A sample TRPL fit is shown for the PEA_2PbI_4 sample.

4. Generalized Elliot model

A generalized version of the Elliott formula was put forward by Lefebvre et al.[3] to treat the Wannier-Mott excitons confined in semiconductor superlattices and quantum wells. This is a versatile approach to account for any anisotropy of a given medium. Earlier, we have used this use this generalized approach for modeling the absorption spectrum from PEA_2PbI_4,[1] and found some deviation from a strictly 2D system, which could be understood as the misorientation of the perovskite planes. By using a non-integer dimension, $\alpha > 1$ for the exciton, the generalized version of the Elliott formula is given by:[3]

$$O(\hbar\omega) = O_0 \left\{ \sum_{n=1}^{\infty} \frac{\mathrm{Ry}^* \Gamma(n+\alpha-2)}{(n-1)!\left[n+\frac{\alpha-3}{2}\right]^{\alpha+1}} \delta(\hbar\omega - E_n) \right.$$

$$+$$

$$\left. \frac{\left|\Gamma\left[\frac{\alpha-1}{2}+i\gamma\right]\right|^2 e^{\pi\gamma}\gamma^{2-\alpha}}{2^{\alpha}\pi^{2-\alpha/2}\Gamma(\alpha/2)} Y(\hbar\omega) \right\}. \quad (S1)$$

The first term in Eq. (S1) represents the excitonic contribution with O_0 being a constant, Ry^* is the effective Rydberg energy related to the binding energy of the exciton, n is the peak order, E_n is the energy of the individual excitonic peak, $\gamma = (\mathrm{Ry}^*/E)^{\frac{1}{2}}$. $\delta(\hbar\omega - E_n)$ is the Dirac delta function which is broadened

by $\frac{1}{a\sqrt{\pi}}e^{-\left(\frac{\hbar\omega-E_n}{a}\right)}$, where a is the broadening parameter. The second term in Eq. (S1) represents the continuum with $Y(\hbar\omega)$ being the Heaviside step function, which is broadened by another parameter b with the form $\frac{1}{1+e^{-2b(\hbar\omega)}}$. We note that for α = 3 and α = 2, Eq. (S2) reduces to its standard from where the continuum is expressed as a hyperbolic sin or cos function.

The absorption spectra of BA_2PbI_4 and PEA_2PbI_4 were modeled by Eq. (S1), and the best agreement with experiment is obtained for α=2.75, as shown in **Fig. S3**. For the strictly 2D case, i.e., α=2, the exciton intensity overshoots the experimental value. The excitonic binding energy (E_B) is related to Ry^* by $\mathrm{E_B} = (-\mathrm{Ry}^*)/[\mathrm{n} + (\alpha - 3)/2]^2$; it is found to be higher for BA_2PbI_4 (144 meV) compared with PEA_2PbI_4 (114 meV).

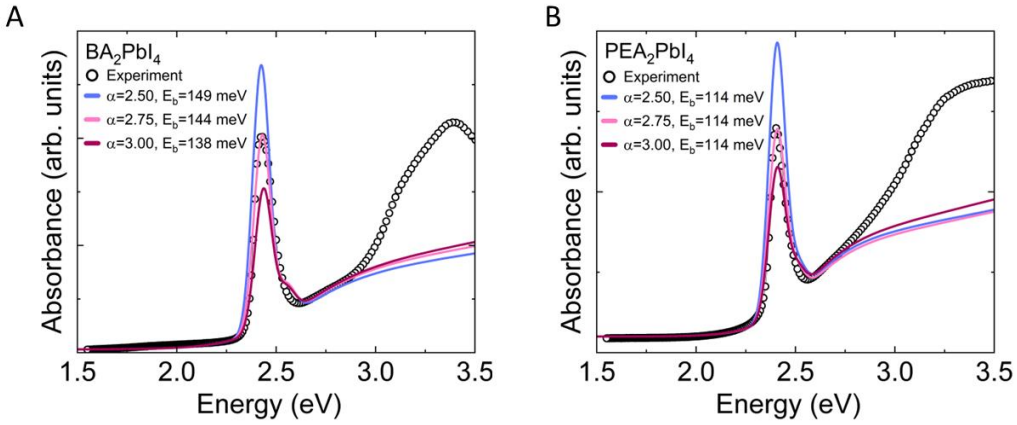

Fig. S3. Simulated absorption spectra for various values of the effective dimensionality (α = 2.5, 2.75, 3) in (A) BA_2PbI_4 and (B) PEA_2PbI_4 using the generalized Elliott formula shown in Eq. S1. The experimental data is shown by the black circles.

5. Estimation of carrier density

We estimate the carrier density (n_0) at a specific pump fluence using the following equation[4]:

$$n_0 = \frac{F\alpha}{h\nu}\,\phi \qquad (S2)$$

where F is the fluence, $h\nu$ is the pump energy, α is the absorption coefficient, and ϕ is the exciton conversion efficiency per photon, which we assume as 1 for PEA_2PbI_4.

Table. S2. Conversion of pump fluence to carrier density in PEA_2PbI_4.

Fluence $\mu J/cm^2$	PEA_2PbI_4 (n_0 $(10^{12}/cm^2)$
47	2.2
72	3.0
111	4.0
144	4.7

6. TA spectra from a 50 nm thick PEA_2PbI_4 film

The data presented in the main manuscript are from ~ 180 nm thick films. As a check, we measured the the TA data from a thinner film (50 nm) of PEA_2PbI_4 grown using CVD. As shown in **Fig. S4**, the TA data is almost identical to the thicker film.

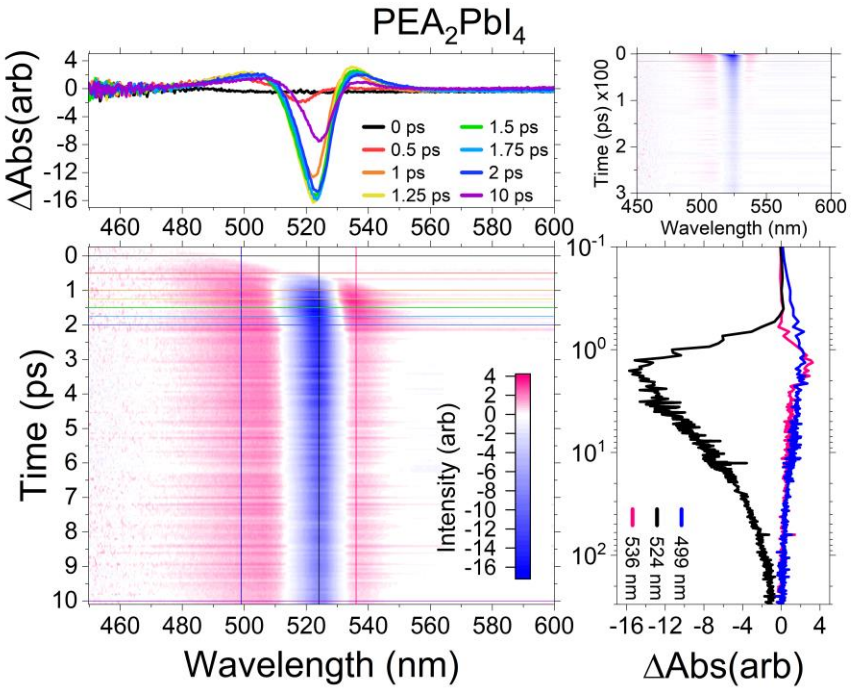

Fig. S4. Transient absorption dynamics of a 50 nm thick PEA_2PbI_4 film. The bottom left panel shows contour maps of the differential absorption changes as a function of time (y-axis) and wavelength (x-axis) in the early timescale until 10 ps. The top panel shows snapshots of ΔA at different times. The right panel shows the time evolution of each peak, where the blue colour represents the high energy absorption peak, black represents the bleaching peak, and pink represents the low energy absorption peak over long time delays. The top right panel shows the contour lines for longer timescale.

7. Decay of the low-energy absorption peak

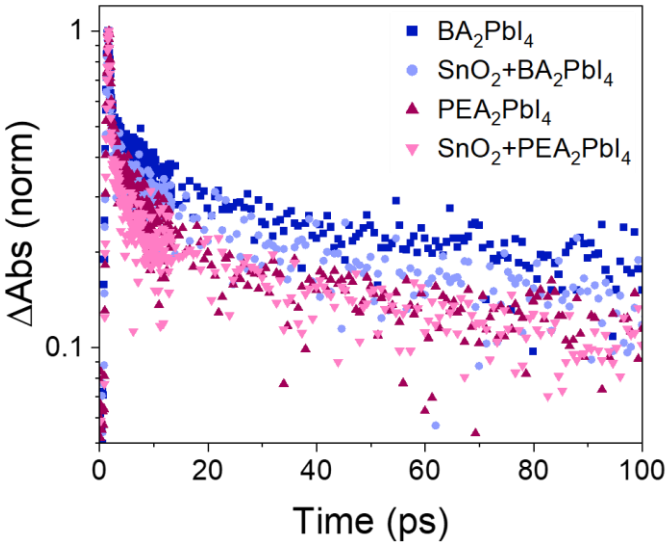

Fig. S5. Decay of the low energy absorption peak normalized for all samples. It is apparent that the low energy absorption peak of the two samples decay differently.

8. Transient absorption spectra of the SnO_2/perovskite heterojunctions.

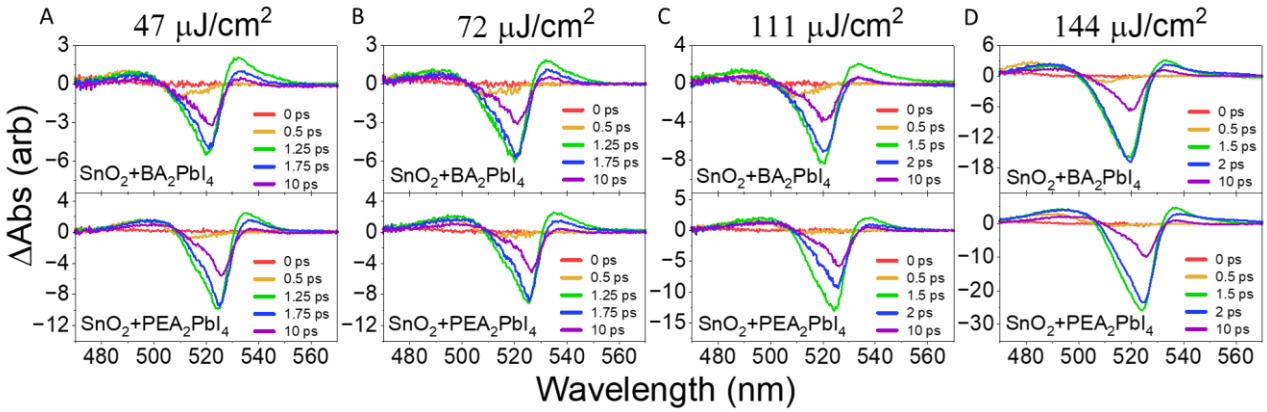

Fig. S6. Transient absorption spectra as function of pump fluence. The 8-panel figure shows the differential absorption spectra for SnO_2/BA_2PbI_4 (Top) and SnO_2/PEA_2PbI_4 (Bottom) at four pump fluences (A) 47 μJ/cm^2, (B) 72 μJ/cm^2, (C) 111 μJ/cm^2, and (D) 144 μJ/cm^2.

9. Decay of the band-edge bleach of the SnO_2/perovskite heterojunctions

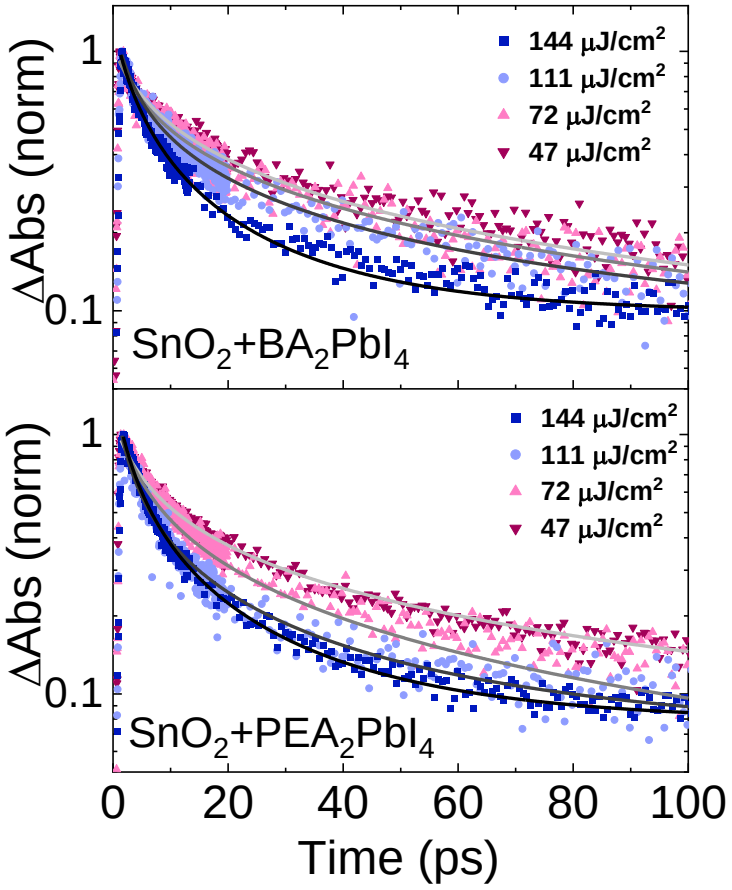

Fig. S7. Normalized ΔA of the bleaching signal in SnO_2/BA_2PbI_4 and SnO_2/PEA_2PbI_4 as a function of the pump fluence. The grey-black lines show the fits for each data set.

10. Fits to the decay of the band-edge bleach of PEA_2PbI_4

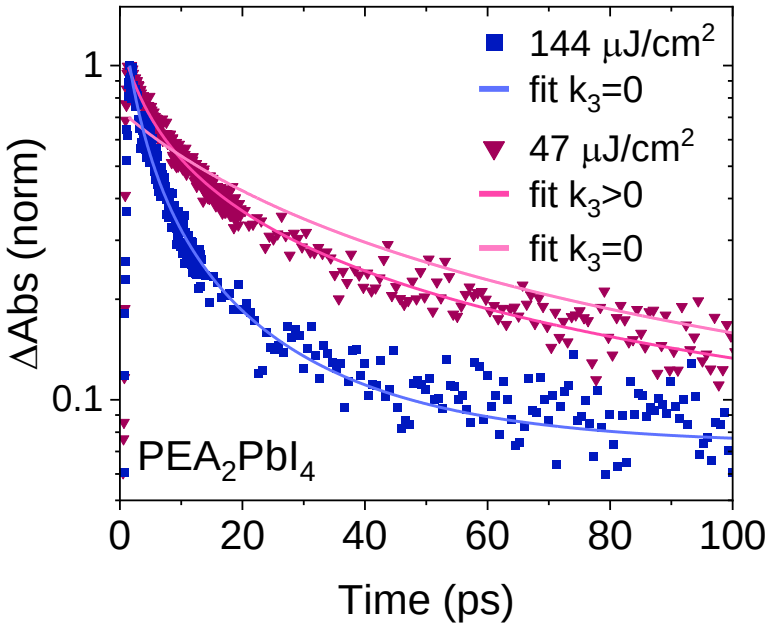

Fig. S8. Fits of the decay of band edge bleach for the PEA_2PbI_4 at highest (144 μJ/cm^2) and lowest (47 μJ/cm^2) fluence with and without using the k_3 term in the fitting parameters.

11. Extracting carrier temperatures

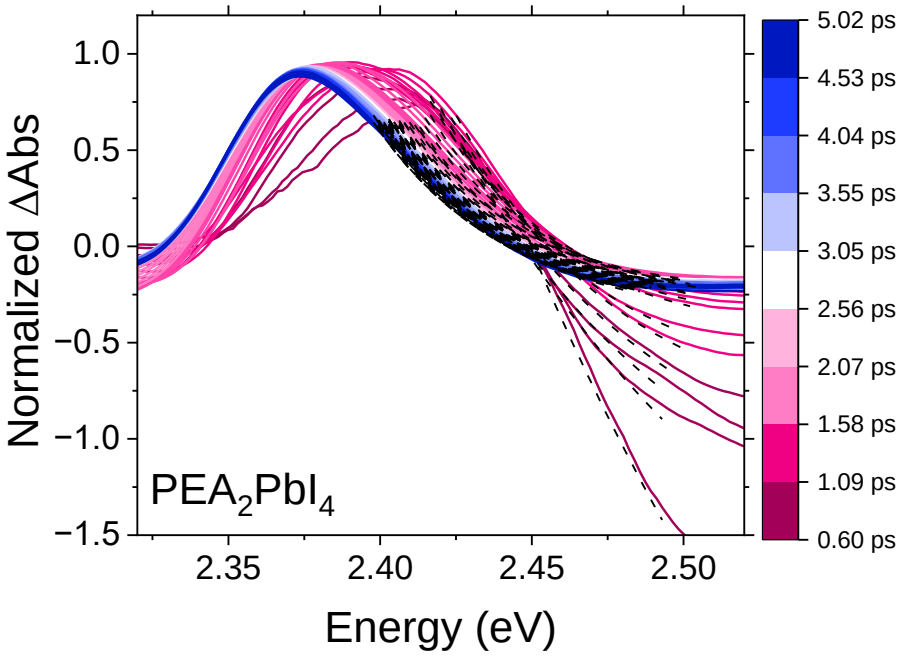

Fig. S9. Normalized ground state bleaching signal of PEA_2PbI_4 in early times (~ 0.6 – 5.0 ps) after photoexcitation by a pump fluence of 144 μJ/cm^2. The colours correspond to different time slices as shown by the colour bar on the right. The black dashed lines show the fits to the high-energy tail of each spectrum between E~2.4 and 2.5eV.

12. Hot carrier cooling in SnO_2/perovskite heterostructures

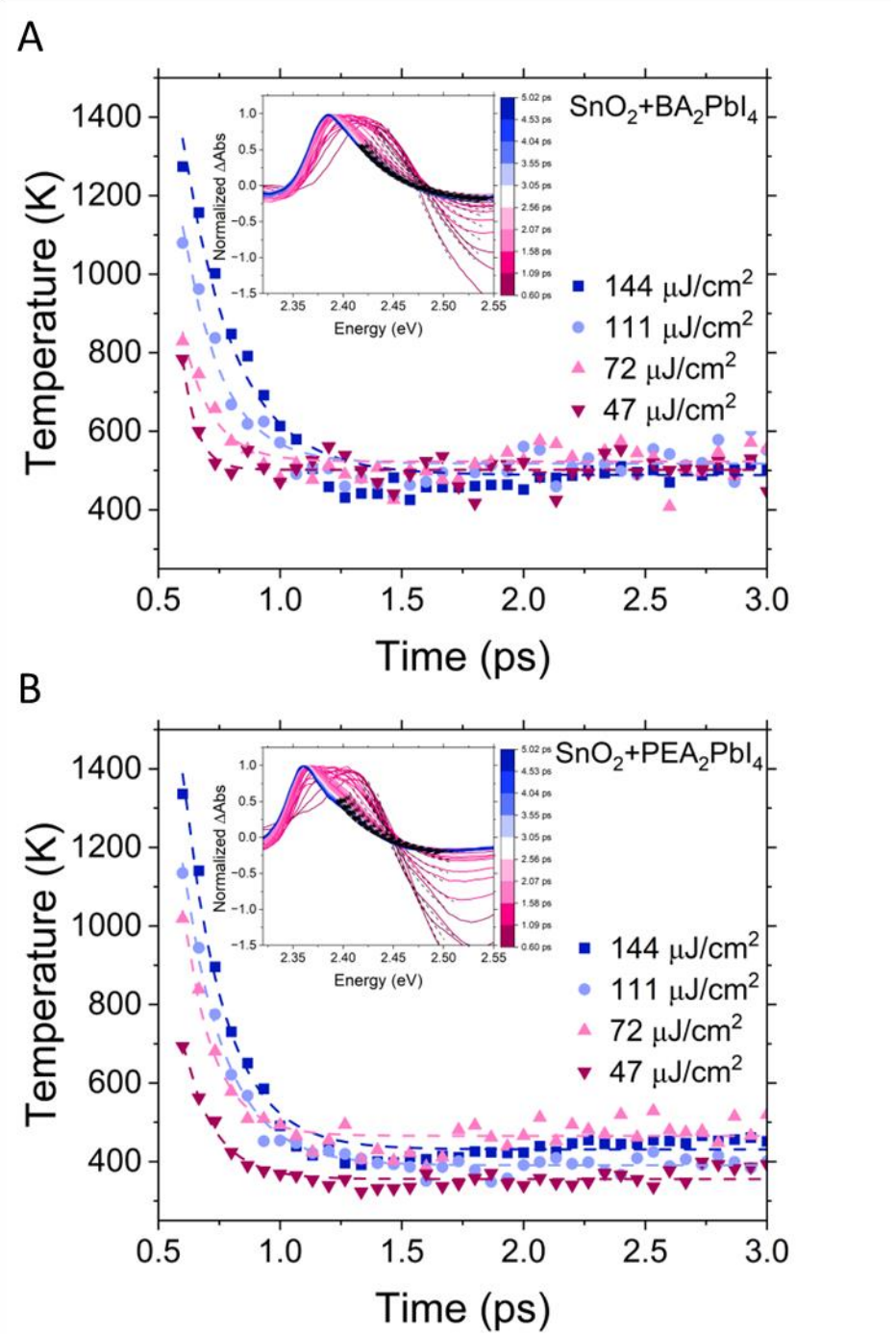

Fig. S10 Photoexcited carrier cooling. A and B Transients of cooling curves (carrier temperature), obtained from Eq. (4), for all pump fluences for SnO_2/BA_2PbI_4 and SnO_2/PEA_2PbI_4, respectively. The dashed lines show fits for an exponential decay in each case. The insets show the normalized TA signal at different time-slices distinguished by different colours and the high-energy tail fits using Eq. (4) are shown by dashed black lines.

References:

1. Arendse, C. J.; Burns, R.; Beckwitt, D.; Babaian, D.; Klue, S.; Stalla, D.; Karapetrova, E.; Miceli, P. F.; Guha, S., Insights into the Growth Orientation and Phase Stability of Chemical-Vapor-Deposited Two-Dimensional Hybrid Halide Perovskite Films. *ACS Appl. Mater. Interfaces* **2023,** 15, (50), 59055-59065.

2. Butler, R.; Burns, R.; Babaian, D.; Anderson, M. J.; Ullrich, C. A.; Morrell, M. V.; Xing, Y.; Lee, J.; Yu, P.; Guha, S., Weak magnetic field-dependent photoluminescence properties of lead bromide perovskites. *J. Appl. Phys.* **2022,** 131, (12).

3. Lefebvre, P.; Christol, P.; Mathieu, H., Unified formulation of excitonic absorption spectra of semiconductor quantum wells, superlattices, and quantum wires. *Phys. Rev. B* **1993,** 48, (23), 17308-17315.

4. Zhang, T.; Zhou, C.; Lin, J.; Wang, J., Regulating the Auger Recombination Process in Two-Dimensional Sn-Based Halide Perovskites. *ACS Photonics* **2022,** 9, (5), 1627-1637.